The Astrophysical Journal, 760:137 (13pp), 2012 December 1 doi:10.1088/0004-637X/760/2/137

COLLISIONLESS SHOCKS IN A PARTIALLY IONIZED MEDIUM. II. BALMER EMISSION

G. Morlino[1], R. Bandiera[1], P. Blasi[1,2], and E. Amato[1]
[1] INAF-Osservatorio Astrofisico di Arcetri, Largo E. Fermi 5, I-50125 Firenze, Italy
[2] INFN, Laboratori Nazionali del Gran Sasso, Assergi (AQ), Italy
Received 2012 July 3; accepted 2012 October 15; published 2012 November 16

ABSTRACT

Strong shocks propagating into a partially ionized medium are often associated with optical Balmer lines. This emission is due to impact excitation of neutral hydrogen by hot protons and electrons in the shocked gas. The structure of such Balmer-dominated shocks has been computed in a previous paper, where the distribution function of neutral particles was derived from the appropriate Boltzmann equation including coupling with ions and electrons through charge exchange and ionization. This calculation showed how the presence of neutrals can significantly modify the shock structure through the formation of a *neutral-induced* precursor ahead of the shock. Here we follow up on our previous work and investigate the properties of the resulting Balmer emission, with the aim of using the observed radiation as a diagnostic tool for shock parameters. Our main focus is on supernova remnant shocks, and we find that, for typical parameters, the Hα emission typically has a three-component spectral profile, where (1) a narrow component originates from upstream cold hydrogen atoms, (2) a broad component comes from hydrogen atoms that have undergone charge exchange with shocked protons downstream of the shock, and (3) an intermediate component is due to hydrogen atoms that have undergone charge exchange with warm protons in the neutral-induced precursor. The relative importance of these three components depends on the shock velocity, on the original degree of ionization, and on the electron–ion temperature equilibration level. The intermediate component, which is the main signature of the presence of a neutral-induced precursor, becomes negligible for shock velocities $\lesssim$1500 km s^{-1}. The width of the intermediate line reflects the temperature in the precursor, while the width of the narrow one is left unaltered by the precursor. In addition, we show that the profiles of both the intermediate and broad components generally depart from a thermal distribution, as a consequence of the non-equilibrium distribution of neutral hydrogen. Finally, we show that a significant amount of Balmer emission can be produced in the precursor region if efficient electron heating takes place.

Key words: acceleration of particles – atomic processes – ISM: supernova remnants – line: profiles

Online-only material: color figures

1. INTRODUCTION

It has been shown (Chevalier & Raymond 1978) that optical spectra dominated by Hα and other Balmer lines, as observed in some historical supernova remnants (SNRs), may arise when an astrophysical shock propagates through a partially ionized medium.

The Balmer emission, observed from these so-called Balmer-dominated shocks, provides a powerful diagnostic tool to investigate the conditions existing in the shock vicinity. The Hα lines typically show two components, resulting from excitation of neutral hydrogen due to the interaction with hot protons and electrons in the shocked gas: a narrow-line component, whose width is characteristic of the cold interstellar medium (ISM) and that has been explained as the result of direct excitation of neutral hydrogen atoms; and a much broader component, associated to a second population of hydrogen atoms, created by charge-exchange (CE) processes between the cold, still unshocked hydrogen and the shocked protons. These hot atoms can be produced in an excited state or can be excited by subsequent collisions with protons or electrons. Hence, the line width of the broad component traces the thermal velocity of shocked protons and can be used to infer the shock velocity. Combining this estimate with proper-motion measurements, one can estimate the distance to the object.

Besides the shock speed, Balmer lines also represent a unique tool to investigate the plasma physics of collisionless shocks. If both narrow and broad components are detected, the relative intensity of the two lines can be used to infer the ratio of electron-to-ion temperature just behind the shock, providing information on the electron–ion equilibration mechanisms (Ghavamian et al. 2007; van Adelsberg et al. 2008).

One of the most intriguing aspects of Balmer emission is related to the possibility of using the line shape and its spatial profile to check the efficiency of SNR shocks in accelerating cosmic rays (CRs). If CR acceleration is taking place in an efficient way, then the widths of both the narrow and broad lines may be affected. In fact, when a sizable fraction of the ram pressure is channeled into non-thermal particles, the plasma temperature behind the shock is expected to be lower, and this should reflect in a narrower width of the broad Hα line. On the other hand, efficient particle acceleration also leads to the formation of a CR-induced precursor upstream, which heats the ionized plasma before the shock. If the precursor is large enough, CE can occur upstream leading to a broader narrow Balmer line. Remarkably, both signatures seem to have been observed in Balmer-dominated shocks. For example, Helder et al. (2009) combined proper-motion measurements of the shock and broad Hα line width for the remnant RCW 86 to demonstrate that the temperature behind the shock is too low, thereby concluding that a sizable fraction of the energy is being channeled into CRs. However, qualitatively similar features can also arise from different physical processes. Therefore, their observation can only be turned into reliable information on the shock properties after a quantitative physical description of the phenomenon is provided.

The basic theory of collisionless shocks in the presence of neutral particles was first developed by Chevalier & Raymond

(1978) and Chevalier et al. (1980) and further refined by Smith et al. (1991) and Ghavamian et al. (2001). These papers were however characterized by similar rather important limitations, mainly due to the assumption that the distribution functions of both populations of neutrals are Maxwellians. In fact, the main difficulty in describing the structure of a collisionless shock propagating in a partially ionized medium is that neutrals have no time to reach thermalization and cannot be treated as a fluid. Steps forward in relaxing the fluid assumption have been made by Heng & McCray (2007) and van Adelsberg et al. (2008) which considered the effect of multiple CE events on the distribution function of hot neutrals. However, these authors limit their calculations to the region downstream of the shock, and consider only the volume-integrated distributions.

A proper description of the effects of the interactions between neutrals and ions on the neutral distribution function requires a fully kinetic approach. This approach has been implemented by Blasi et al. (2012, hereafter Paper I) where we derived simultaneously the neutral distribution function and the hydrodynamic quantities for ions (which are, instead, treated as a fluid), both upstream and downstream of the shock, by solving a Boltzmann equation including CE and ionization terms. The main result of Paper I is that of providing a mathematical and physical description of what we call the *neutral return flux*: when fast, cold neutrals undergo CE interactions with the slower hot ions downstream of the shock, some fraction of the resulting hot neutrals can cross the shock and move upstream. The relative velocity between these hot neutrals and the upstream ions triggers the onset of CE and ionization interactions that lead to the heating and slowing down of the ionized component of the upstream fluid. The system then tends to develop a shock precursor, in which the fluid velocity gradually decreases from its value at upstream infinity, and even more important, the temperature of ions in the upstream region increases as a result of the energy and momentum deposition of returning neutrals.

The existence of a neutral return flux from downstream to upstream was previously mentioned by Smith et al. (1994) and Hester et al. (1994) as a possible way to explain the anomalous width of narrow Balmer lines observed in some SNRs (see, e.g., Sollerman et al. 2003), but no explicit calculation was carried out.

The width of such lines is in the 30–50 km s^{-1} range, implying a pre-shock temperature around 25,000–50,000 K. If this were the ISM equilibrium temperature there would be no atomic hydrogen, implying that the pre-shock hydrogen is heated by some form of shock precursor in a region that is sufficiently thin so that collisional ionization equilibrium cannot be established before the shock. Several mechanisms have been proposed to explain the broadening of the narrow line (see Heng 2009, for a review), but most of them can be ruled out on theoretical grounds, leaving a CR precursor and/or a neutral precursor as the most probable origin.

A first attempt at investigating the broadening of the narrow-line component induced by the neutral precursor was made by Lim & Raga (1996), using a simplified Boltzmann equation for neutrals in one dimension in both physical and velocity space. The calculations were carried out for a shock speed of 225 km s^{-1}, and varying the initial ionization fraction from 0.5 to 0.99. The narrow line width does not show any appreciable change due to the return flux.

In the present work, we use the theory developed in Paper I and calculate the profile of Balmer line emission in the presence of neutral return flux. In particular, we show that the neutral return flux is responsible for the emission of a third intermediate line component, in addition to the narrow and broad ones. This intermediate line is produced by hydrogen atoms that have undergone CE with warm protons in the neutral precursor. Interestingly, there are observations which suggest the existence of such intermediate component (Ghavamian et al. 2000), although the results might also be due to projection effects since the emission region is morphologically rather complex. At the present time, spectral and spatial information are not sufficient to disentangle the physical effect that we describe here from geometrical and projection effects which could modify the line profiles. We also show that the neutral-induced precursor is not able to broaden the width of narrow Hα line, confirming the first finding of Lim & Raga (1996).

The paper is organized as follows: in Section 2 we summarize the kinetic approach developed in Paper I and use it to describe the shock structure in the presence of neutrals. We improve on previous work by both adding electrons in the shock dynamics and including their contribution to the ionization of neutrals. In Section 3 we write down the basic equations for the calculation of the Balmer line emission, and in Section 4 we illustrate the main results in terms of spatial profiles of the total emission, of line profile, as well as line intensity ratios. We also compare theoretical profiles with profiles obtained by simulated observations, in order to derive the observational requirements necessary in order to be able to detect the intermediate component, and deviations from Gaussianity in general. We conclude in Section 5.

2. PHYSICAL MODEL

The basic model we consider consists of a plane-parallel shock with velocity $V_{\rm sh}$ that propagates into a partially ionized proton–electron plasma along the z-direction, with a given fraction of neutral hydrogen at upstream infinity. We neglect the presence of helium and other heavier chemical elements.

Protons and electrons are assumed to behave as fluids with temperatures $T_i(z)$ and $T_e(z)$, respectively, with the same bulk velocity, $v_i(z) = v_e(z)$, and the same number density, $n_i(z) = n_e(z)$. Their distribution functions, $f_i(\boldsymbol{v}, z)$ and $f_e(\boldsymbol{v}, z)$, are assumed to be Maxwellian at each position z. Neutral hydrogen interacts with protons and electrons through CE and ionization. The hydrogen distribution function, $f_N(\boldsymbol{v}, z)$, can be described using the Boltzmann equation

$$\frac{\partial f_N}{\partial t} + \boldsymbol{v}\cdot\nabla f_N = \beta_N f_i - \beta_i f_N - \beta_e f_N, \qquad (1)$$

where the collision terms $\beta_k f_l$ represent the interaction (due to CE and ionization) between the species k and l. The interaction rate β_k is formally written as

$$\beta_k(\boldsymbol{v}, z) = \int d^3w\, v_{\rm rel}\, \sigma(\boldsymbol{v}_{\rm rel}) f_k(\boldsymbol{w}, z), \qquad (2)$$

where $v_{\rm rel} = |\boldsymbol{v} - \boldsymbol{w}|$ and σ is the cross section for the interaction process. More precisely, β_N is the rate of CE of an ion that becomes a neutral, β_i is the rate of CE plus ionization of a neutral due to collisions with protons, while β_e is the ionization rate of neutrals due to collisions with electrons. Equation (1) is used to calculate f_N starting from the distribution of charged species (protons and electrons), under the assumption of stationarity ($\partial f_N/\partial t = 0$).

The dynamics of protons and electrons coupled with neutrals can be described very generally through conservation equations

of mass, momentum, and energy:

$$\frac{\partial}{\partial z}\left[(\rho_i+\rho_e)v_i+F_{\rm mass}\right]=0, \quad (3)$$

$$\frac{\partial}{\partial z}\left[(\rho_i+\rho_e)v_i^2+P_i+P_e+F_{\rm mom}\right]=0, \quad (4)$$

$$\frac{\partial}{\partial z}\left[\frac{1}{2}(\rho_i+\rho_e)v_i^3+\frac{\gamma_g(P_i+P_e)v_i}{\gamma_g-1}+F_{en}\right]=0, \quad (5)$$

where $F_{\rm mass}=m_{\rm H}\int d^3v v_\parallel f_N$, $F_{\rm mom}=m_{\rm H}\int d^3v v_\parallel^2 f_N$, and $F_{en}=m_{\rm H}/2\int d^3v v_\parallel(v_\parallel^2+v_\perp^2)f_N$ are respectively the fluxes of mass, momentum, and energy of neutrals along the z-direction. Usually the dynamical role of electrons is neglected due to their small mass. However, collective plasma processes could contribute to equilibrate electron and proton temperatures to some level. If this equilibration is very efficient, then the electron pressure can no longer be neglected and the total gas pressure needs to include both proton and electron contributions, namely, $P_g=P_i+P_e=P_i(1+\beta)$, where $\beta(z)\equiv T_e/T_i$ is the electron to proton temperature ratio and is taken as a free parameter.

The solution of Equations (1)–(5) is described in detail in Paper I. The only difference here is the presence of electrons, which has been previously neglected because it does not affect the shock dynamics, unless $T_e\sim T_i$. The importance of introducing the electron contribution in this context comes from the fact that Balmer emission is very sensitive to both T_e and T_i (Heng & McCray 2007; van Adelsberg et al. 2008). Therefore, even very partial equilibration can produce observational consequences in the line emission, as we show in Section 4.

The level of electron–ion equilibration is one of the open questions in collisionless shock physics and Hα observations present us with a unique tool to investigate this aspect. Theoretically the equilibration process is far from being understood and anything between total absence of interaction and full equilibration (FE) has been proposed (see Rakowsky 2005, for a review). Moreover the electron–ion equilibration level is expected to change between upstream and downstream of the shock because the plasma conditions in these two regions are totally different in terms of temperature and turbulence properties. As a consequence, we distinguish between upstream and downstream using two separate parameters, $\beta_{\rm up}$ and $\beta_{\rm down}$, respectively.

We stress that a crucial assumption of our calculation is that new protons produced at position z by CE and ionization instantly thermalize with other protons. As discussed in Paper I, such an assumption, which is especially important in the upstream region, is rather delicate: protons might isotropize and yet not thermalize with the rest of protons in the plasma. A dedicated effort using numerical particle simulations should be used to address this important issue.

In principle, the dynamics of electrons in the upstream region could also be affected by electrons ejected due to the ionization of neutrals that have returned upstream. This effect can however be neglected for the calculation of Balmer lines: in Paper I we showed that the fraction of returning neutrals is $\lesssim$5%. Let us assume that all these neutrals are ionized in the upstream region. To a good approximation, stripped electrons can be expected to have the same velocity of their parent atoms, which, in turn, have a mean velocity of the order of the downstream proton thermal speed. Hence, the temperature of stripped electrons is $T_{e,\rm in}\simeq 3/8V_{\rm sh}^2 m_e/k_B\approx 6.2\times10^5(V_{\rm sh}/5000\ {\rm km\ s^{-1}})^2$ K. Now, assuming that the newly generated electrons reach equilibrium with preexisting electrons, the final temperature is of the order of $(n_0T_0+n_{\rm in}T_{\rm in})/(n_0+n_{\rm in})\approx 2.5\times10^4$ K, where we use $V_{\rm sh}=5000$ km s^{-1} and an initial ionization fraction of 50%. This temperature is too low to be relevant for Balmer emission. In fact, electrons can contribute only if their velocity is $\gtrsim$2000 km s^{-1}, namely, if $T_e\gtrsim10^5$ K.

3. CALCULATION OF BALMER LINE EMISSION

Once the distribution functions of hydrogen, protons, and electrons are known at each position, the calculation of line emission is quite straightforward, provided that the relevant cross sections are known. Here we concentrate on the Balmer Hα line, which results from the hydrogen deexcitation from level $3s$ and $3d$ to $2p$ as well as from $3p$ to $2s$. The latter case is complicated by the fact that the $3p$ level can also decay into $1s$, producing Lyβ photons. Depending on the optical depth of the medium, these photons can either escape the system or be reabsorbed by ground-state hydrogen and eventually reemitted as Hα photons. In the literature the optically thin and optically thick cases are usually labeled as Case A and Case B, respectively, and the total Hα production rate is written as

$$R_{\rm H\alpha}=R_{\rm H(3s)}+R_{\rm H(3d)}+B_{3p,2s}R_{\rm H(3p)}, \quad (6)$$

where $R_{\rm H(3l)}$ is the production rate of hydrogen excited at level $3l$ and the factor $B_{3p,2s}$ is the fraction of transitions from $3p$ to $2s$, which is ≈0.12 in the optically thin case (Case A) while it becomes unity in the optically thick case (Case B) (van Adelsberg et al. 2008).

The conversion efficiency from Lyβ to $H\alpha$ photons depends on the shock speed, the electron–ion temperature ratio, and the pre-shock ionization fraction. It was first computed by Chevalier et al. (1980), who found that in conditions appropriate for many Balmer-dominated shocks the emission from cold hydrogen is generally optically thick while the emission from hot hydrogen is close to be optically thin. In this work, following that result, we adopt $B_{3p,2s}=0.12$ (1) for the emission produced by hot (cold) hydrogen.

In order to calculate the Hα emission for both Case A and Case B, we need to compute the different production rates of hydrogen excited to the sublevels $3s$, $3p$, and $3d$. The excited hydrogen is mainly produced by two different processes: collisions with protons and electrons, and CE reactions leaving the hydrogen atom in an excited state. For the sake of clarity here we neglect further contributions due to collisions with helium. The production rate of $H(3l)$ at a fixed position z reads

$$\begin{aligned}R_{\rm H(3l)}(\boldsymbol{v},z)=&\int d^3w\, v_{\rm rel}\, f_{\rm H}(\boldsymbol{v},z)\\ &\times\left[f_i(\boldsymbol{w},z)\,\sigma_{{\rm ex}(i)}^{{\rm tot}(3l)}(v_{\rm rel})+f_e(\boldsymbol{w},z)\,\sigma_{{\rm ex}(e)}^{{\rm tot}(3l)}(v_{\rm rel})\right]\\ &+\int d^3w\, v_{\rm rel}\, f_i(\boldsymbol{v},z)f_{\rm H}(\boldsymbol{w},z)\,\sigma_{\rm ce}^{{\rm tot}(3l)}(v_{\rm rel}). \quad (7)\end{aligned}$$

Note that the hydrogen distribution function $f_{\rm H}$ includes only atoms at the ground level $1s$. In fact, collisional deexcitation can be neglected because it occurs on a typical time scale $\tau_{\rm coll}\simeq(n_i\sigma_{\rm coll}V_{\rm sh})^{-1}\simeq10^7$ s (for $n_i=1$ cm^{-3} and $V_{\rm sh}=1000$ km s^{-1}) which is much longer than spontaneous deexcitation, whose timescale (from state n to state m) is $\tau=\hbar/\Delta E=4.8\times10^{-15}(n^{-2}-m^{-2})$ s. Hence, atoms decay to the ground state before undergoing any further collision.

In Equation (7), we use the total excitation and CE cross sections for the atomic sublevel $3l$, $\sigma_{\rm ex}^{{\rm tot}(3l)}$ and $\sigma_{\rm ce}^{{\rm tot}(3l)}$, which

take into account the direct excitation processes, $1s \rightarrow 3l$, plus contributions coming from atoms excited to higher levels with $n > 3$ that subsequently decay to the state $3l$. Formally this total cross section can be written in the following form:

$$\sigma^{\mathrm{tot}(3l)} = \sum_{n',l'}^{\infty} B_{n'l',3l}\, \sigma_{1s\rightarrow n'l'}. \quad (8)$$

where $\sigma_{1s\rightarrow n'l'}$ is the cross section for excitation from the ground state to the level $n'l'$ and the $B_{n'l',nl}$ are the cascade matrix elements representing the probability that a hydrogen atom excited to state $n'l'$ will make a transition to state nl (with $n < n'$) via all cascade routes.

We treat CE, excitation and ionization between electrons, protons, and hydrogen atoms using the cross sections of Barnett el al. (1990), Belkić et al. (1992), Janev & Smith (1993), Balança et al. (1998), and Harel et al. (1998).[3] For some of these cross sections we adopt the fitting functions provided by Heng & Sunyaev (2008) and Tseliakhovich et al. (2012). At the time of writing, the CE cross sections for sublevels with different angular momentum states are known only up to the level $n = 4$. We estimate that neglecting the contribution of higher levels entails an error around 5% in the calculation of the total σ_{ce}, therefore in the following we ignore levels with $n > 4$. Hence, for the CE process, the cross sections reduce to the following:

$$\sigma_{\mathrm{ce}}^{\mathrm{tot}(3s)} \simeq \sigma_{\mathrm{ce},1s\rightarrow 3s} + B_{4p,3s}\, \sigma_{\mathrm{ce},1s\rightarrow 4p}, \quad (9)$$

$$\sigma_{\mathrm{ce}}^{\mathrm{tot}(3d)} \simeq \sigma_{\mathrm{ce},1s\rightarrow 3d} + B_{4d,3d}\, \sigma_{\mathrm{ce},1s\rightarrow 4d}, \quad (10)$$

$$\sigma_{\mathrm{ce}}^{\mathrm{tot}(3p)} \simeq \sigma_{\mathrm{ce},1s\rightarrow 3p} + B_{4s,3p}\, \sigma_{\mathrm{ce},1s\rightarrow 4s} + B_{4d,3p}\, \sigma_{\mathrm{ce},1s\rightarrow 4d}, \quad (11)$$

where we use the values of $B_{4l',3l}$ as listed by Heng & Sunyaev (2008) (see their Table 3). An identical approach is adopted to calculate the impact excitation by protons, restricted to levels 3 and 4. We adopt the impact excitation cross sections calculated by Balança et al. (1998) and Tseliakhovich et al. (2012) for the sublevels $3l$ and $4l$, respectively. Unfortunately, these works provide cross sections only for a limited range of impact energies, 1–100 keV and 5–80 keV, respectively, which means that the relative speed between protons and hydrogen atoms can be respectively in the range $[v_1, v_2] = [438, 4377]$ km s^{-1} and [978, 3914] km s^{-1}. Outside these velocity ranges we estimate the sublevel cross sections, $\sigma_{\mathrm{ex}(i)}^{nl}$, using the total cross sections, $\sigma_{\mathrm{ex}(i)}^{n}$ as taken from Janev & Smith (1993), in the following way:

$$\sigma_{\mathrm{ex}(i)}^{nl}(v > v_2) = \sigma_{\mathrm{ex}(i)}^{n}(v)\frac{\sigma_{\mathrm{ex}(i)}^{nl}(v_2)}{\sigma_{\mathrm{ex}(i)}^{n}(v_2)}\,(1+\epsilon_n)\,, \quad (12)$$

where the coefficients ϵ_n are chosen in such a way as to have $\sum_l \sigma_{nl}(v_{1(2)}) = \sigma_n(v_{1(2)})$, and their values are of the order of few percent. A similar approximation has been used also for $v < v_1$.

Also the impact excitation by electrons is limited to sublevels $3l$ and $4l$ and expressions similar to Equations (9)–(11) hold for $\sigma_{\mathrm{ex}(e)}^{\mathrm{tot}(3l)}$ as well. In this case we use the cross sections provided by Bray & Stelbovics (1995), computed using the convergent close-coupling method. As for the previous case, the error in the total cross section produced by excluding higher excited levels is around 5%.

In order to compute the spatial emissivity profile of the Hα emission, we need to integrate Equation (6) in the velocity directions orthogonal to the line of sight. From the observational point of view, most cases refer to shocks viewed edgewise because of limb brightening. In such cases, assuming a pure plane shock (i.e., neglecting curvature effects), the edgewise emissivity profile results from the following integration:

$$\begin{aligned} F_{\mathrm{H}\alpha}(z, v_x) &= \int\int dv_z dv_y \left[R_{\mathrm{H}(3s)}(z, \boldsymbol{v}) + R_{\mathrm{H}(3d)}(z, \boldsymbol{v}) + B_{3p,2s} R_{\mathrm{H}(3p)}(z, \boldsymbol{v})\right] \\ &= 2\int_{-\infty}^{\infty} dv_z \int_{v_x}^{\infty} \frac{dv_\perp}{\sqrt{1-(v_x/v_\perp)^2}} \left[R_{\mathrm{H}(3s)}(z, v_z, v_\perp) + R_{\mathrm{H}(3d)}(z, v_z, v_\perp) + B_{3p,2s} R_{\mathrm{H}(3p)}(z, v_z, v_\perp)\right], \end{aligned} \quad (13)$$

where z is the direction of shock propagation, x is the direction along the line of sight, and y is orthogonal to the (x, z) plane. In the second equality we use $v_\perp \equiv (v_x^2 + v_y^2)^{1/2}$. Starting from Equation (13) we can obtain more useful integrated quantities, which can be directly compared with observations, namely, the spatial emissivity profile, $\xi_{\mathrm{H}\alpha}(z)$, the volume-integrated line profile, $\phi_{\mathrm{H}\alpha}(v_x)$, and the total line strength, $I_{\mathrm{H}\alpha}$, respectively defined as

$$\begin{aligned} \xi_{\mathrm{H}\alpha}(z) &= \int_{-\infty}^{\infty} dv_x\, F_{\mathrm{H}\alpha}(z, v_x), \\ \phi_{\mathrm{H}\alpha}(v_x) &= \int_{-\infty}^{\infty} dz\, F_{\mathrm{H}\alpha}(z, v_x), \ \text{and} \\ I_{\mathrm{H}\alpha} &= \int\int dv_x dz\, F_{\mathrm{H}\alpha}(z, v_x). \end{aligned} \quad (14)$$

In the next section, we will investigate how these observables can be used to test the presence of a neutral-induced precursor and to infer the ambient parameters (as the ionization fraction, the shock speed and the electron–proton equilibration level).

4. RESULTS

In this section, we illustrate the main results of our kinetic calculation concerning the Hα emission. It is well known that Balmer emission is highly sensitive to plasma density, shock velocity, initial degree of ionization, and electron–ion equilibration level. Our aim is to illustrate how to disentangle different effects produced by these quantities. The main observable quantities are the spatial profile, the line profile, and the relative intensity of the broad and narrow lines. Below we discuss the interpretation of these quantities and their relation with physical parameters, comparing our results with previous work.

For all cases discussed, we fix the temperature at upstream infinity to 10^4 K, because larger values are incompatible with the presence of neutral hydrogen, while for lower values the results do not change significantly. Also the total upstream numerical density is fixed to $n_{\mathrm{tot}} = 0.1$ cm^{-3}, while the plasma ionization fraction is assumed to be 50%, unless otherwise specified. We notice that the total density can be factorized out in Equations (1)–(5), hence a change in the total density only reflects in a change of the length scales of the problem, while all other quantities remain unchanged.

[3] Many of these cross sections can be found in the International Atomic Energy Agency Web site: http://www-amdis.iaea.org/ALADDIN/

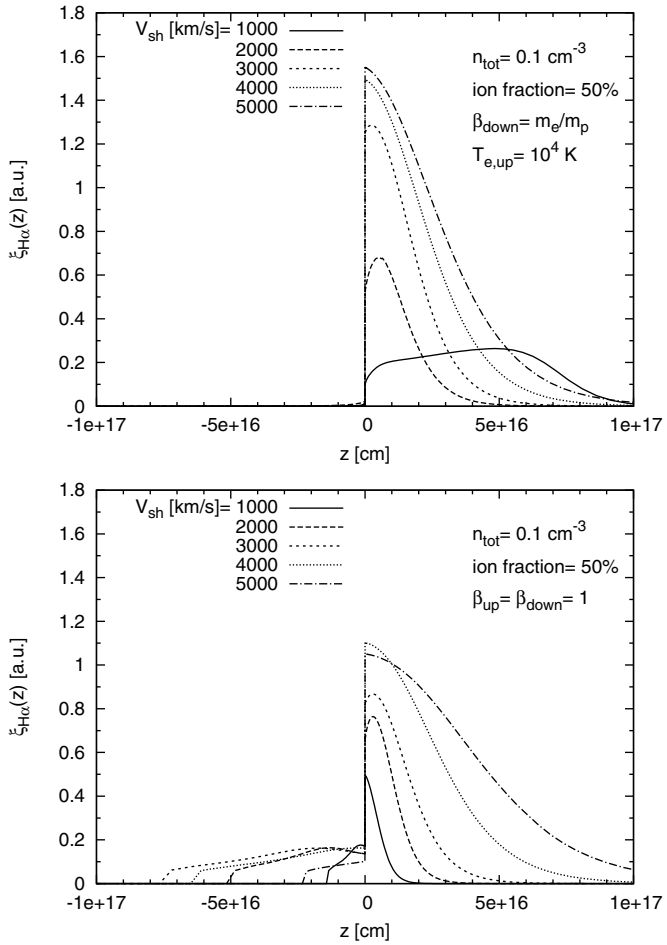

Figure 1. Spatial emissivity profile of the Hα line for $n_{\rm tot} = 0.1$ cm^{-3}, 50% ionization fraction and for different values of shock velocity, as specified in each panel. Two extreme cases of electron–ion temperature equilibration are shown: NE (upper panel) and FE (lower panel), i.e., $\beta_{\rm up} = \beta_{\rm down} = 1$.

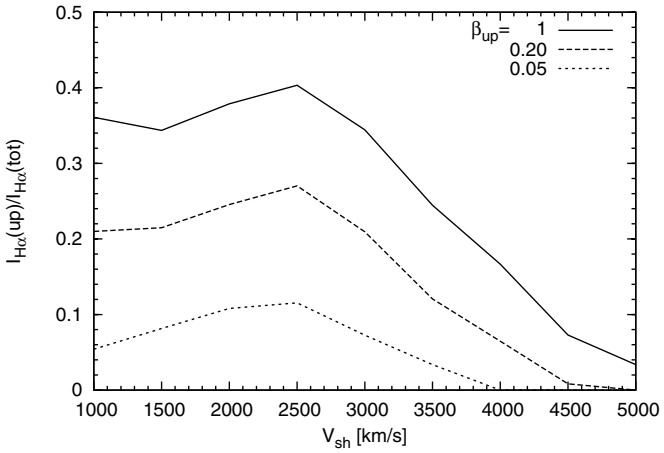

Figure 2. Fraction of the total emissivity coming from the upstream as a function of shock velocity and for three different assumptions on the degree of electron–proton equilibration upstream ($\beta_{\rm down}$ is fixed to 1 for all cases).

As we already pointed out, the electron-to-proton equilibration level, β, is expected to change between upstream and downstream of the shock, hence we use two independent parameters, $\beta_{\rm up}$ and $\beta_{\rm down}$, respectively. We will focus mainly on the two extreme cases of FE, where protons and electrons share the same temperature everywhere (i.e., $\beta_{\rm up} = \beta_{\rm down} = 1$) and no equilibration (NE) at all, which corresponds to the situation where electrons and protons do not interact at all. In the latter case, the electron temperature is equal to 10^4 K in the entire upstream region and $\beta_{\rm down} = m_e/m_p$ in the downstream. Intermediate equilibration cases will be also discussed.

4.1. Spatial Emission

Figure 1 shows the spatial emissivity profile, $\xi_{\rm H\alpha}(z)$, for different shock velocities and for the two extreme assumptions for the electron–ion equilibration efficiency: the upper panel shows the NE case, while the lower panel shows the FE case. Interestingly, while in the former case the emission is produced only in the downstream, in the latter case a substantial fraction of the Hα emission comes from the upstream. This fact is better illustrated in Figure 2, where the fraction of total Hα emission produced upstream is plotted as a function of shock velocity and for different values of electron–ion equilibration efficiency upstream (while $\beta_{\rm down}$ is fixed to 1): the upstream emission has a peak when $V_{\rm sh}$ is close to 2500 km s^{-1} and can reach $\sim$40% of the total emission when $\beta_{\rm up} = 1$. Remarkably, even reducing $\beta_{\rm up}$ down to 0.05, the upstream emission is still a non-negligible fraction of the total, being around 10%. For velocities $>$2500 km s^{-1} the upstream emission decreases monotonically because the heating produced by the neutral return flux becomes less efficient, as shown in Paper I (see its Figure 6).

The Hα emission produced upstream is clearly due to collisional excitation of hydrogen by electrons. In fact, this process has a threshold for $v_{\rm rel} \simeq 2000$ km s^{-1} and peaks at $v_{\rm rel} \simeq 3000$ km s^{-1}, hence when the electron temperature is larger than $\simeq 1.5 \times 10^5$ K the atomic level $n = 3$ is easily excited and Hα emission is produced. On the other hand, excitation produced upstream by protons is suppressed because, for a given common temperature, protons have a thermal speed $\sqrt{m_e/m_p}$ times lower than electrons; hence, Hα emission induced by proton collisions and CE becomes relevant only for $T_p \gtrsim$ few $\times 10^7$ K. The heating induced by the neutral return flux may lead to such ion temperatures upstream, but only very close to the shock, on spatial scales that are too small to affect the Hα emission.

From Figure 1 we can see that Hα emission seems to increase with increasing shock velocity. This is a consequence of the fact that the production efficiency of Hα photons is almost constant at high $V_{\rm sh}$. This is shown in Figure 3 where we plot the efficiency of Hα emissivity, defined as the number of Hα photons emitted per hydrogen atom crossing the shock, namely, $\epsilon = I_{\rm H\alpha}/(V_{\rm sh} n_{\rm H,0})$, where $n_{\rm H,0}$ is the hydrogen number density at upstream infinity. In Figure 3 several cases are shown: the solid and dotted thick lines refer to NE and FE cases, respectively, while the dot-dashed thick line refers to an intermediate case (NE upstream and partial equilibrium downstream with $\beta_{\rm down} = 0.1$). For all these three cases we assumed that the plasma is optically thin to Lyβ emission from hot hydrogen atoms (Case A) and optically thick to Lyβ emission from cold hydrogen (Case B) as discussed at the beginning of Section 3. In order to compare our results with previous work, we also plot the cases where the plasma is optically thin or optically thick for both the hot and the cold hydrogen emission, but only for the NE case.

These latter two cases can be compared with the estimated efficiency provided by Chevalier & Raymond (1978) who give $\epsilon_A = 0.048$ and $\epsilon_B = 0.27$, independently of the shock velocity. We note that while ϵ_B is quite close to our finding, especially for

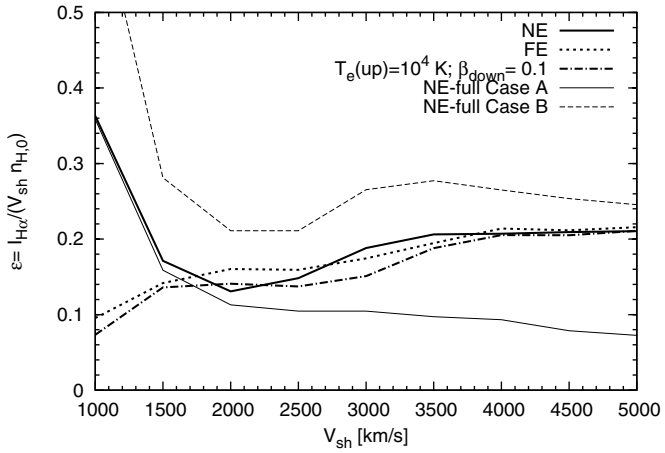

Figure 3. Efficiency of the Hα emission (i.e., number of photons emitted for each hydrogen atom crossing the shock) as a function of the shock velocity and for different degrees of electron–ion equilibration efficiency. The thick lines refer to the cases of non-equilibrium (solid), full equilibrium (dotted), and partial equilibrium with $\beta_{\rm down} = 0.1$ (dot-dashed). For these cases the plasma is assumed to be optically thin for Lyβ photons produced by hot hydrogen atoms, but optically thick for photons produced by cold hydrogen atoms. The thin lines, instead, show NE cases assuming a medium that is either optically thin (Case A) or optically thick (Case B) to Lyβ photons.

high shock speed, the value of ϵ_A is about a factor two smaller than our result. The discrepancy is probably due to the fact that the excitation cross sections used at that time were not very accurate.

4.2. Hα Line Profile

Let us now analyze the shape of Hα lines. Figure 4 shows the volume-integrated line profiles, $\phi_{\rm H\alpha}(v_x)$, for several values of the shock velocity, for both NE (upper panel) and FE (lower panel) cases. Several comments are in order. The first point to note is that $\phi_{\rm H\alpha}$ cannot be described, in general, by only two Gaussian-like components, as usually assumed in the literature. Besides the usual narrow and broad components, we clearly see the presence of a third intermediate component whose typical width is about few hundreds km s^{-1}. This intermediate component is a direct consequence of the existence of the neutral-induced precursor. In fact, as we showed in Paper I, the neutral return flux can heat upstream protons up to a temperature $\sim 10^6$–10^7 K. Hence, hydrogen atoms that undergo CE upstream with these warm protons can produce Hα emission with a typical width of $\sim$100 km s^{-1}. This picture also suggests that the intermediate component should have a non-Gaussian profile because it contains contributions from hydrogen populations at different locations in the precursor, which have different temperatures.

This physical interpretation of the intermediate component is supported by the fact that its intensity, with respect to the narrow line, increases or decreases according to the temperature and length of the neutral precursor. For example, in Figure 5 we show the effect of increasing the initial neutral fraction from 1% to 50%. We see that the intermediate component becomes more prominent as the neutral fraction increases: this is a consequence of the fact that the heating-induced upstream by the neutral return flux increases. A similar behavior occurs when changing the shock speed. In Paper I, we showed that the upstream temperature has a maximum for $V_{\rm sh} \simeq 2000$ km s^{-1} and decreases for smaller and larger speeds. The same happens

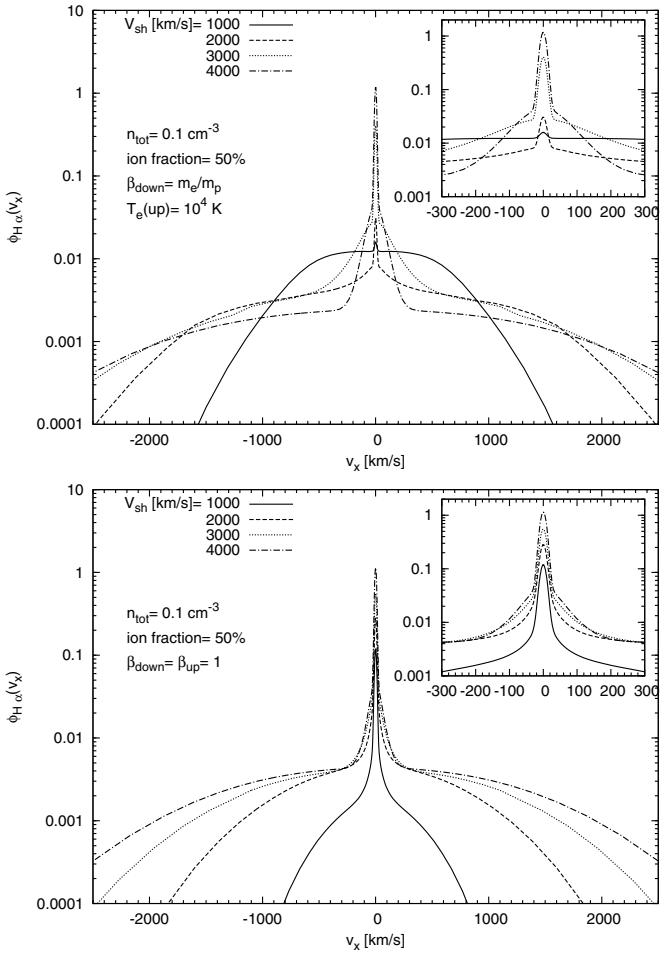

Figure 4. Volume-integrated Hα emission for different values of the shock velocity. The upper and lower panels show the cases NE and the FE cases, respectively. The values of total density and ionization fraction are the same as in Figure 1. The small boxes show a zoom for small values of v_x, aimed at emphasizing the shape of the narrow and intermediate lines.

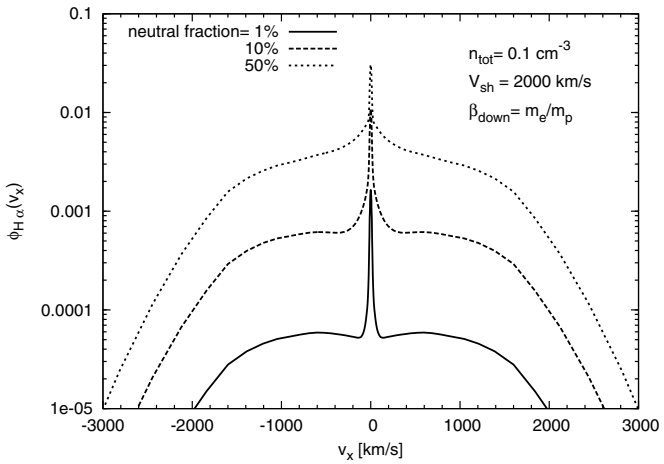

Figure 5. Volume-integrated Hα emission for three different values of upstream ionization fraction.

for the emission of the intermediate component with respect to the narrow one (see Figures 8 and 9).

The variation of electron–ion equilibration efficiency also considerably affects the line profile. In Figure 6, we plot $\phi_{\rm H\alpha}$ for a fixed shock speed and for different values of $\beta_{\rm down}$. When $\beta_{\rm down}$ increases, a decreasing of the broad emission is

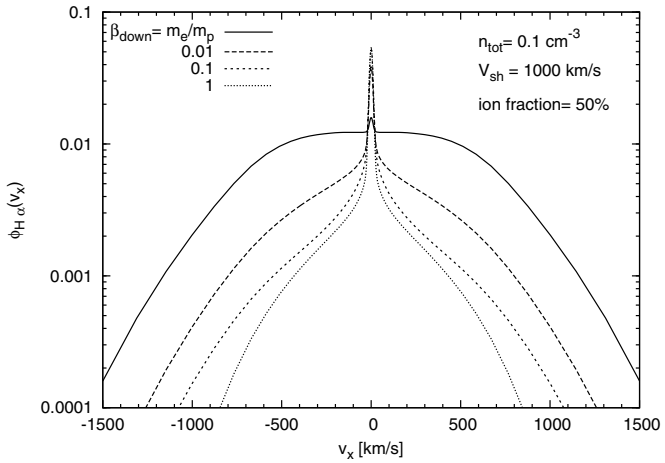

Figure 6. Volume-integrated Hα emission for different values of the downstream electron–ion equilibration efficiency $\beta_{\rm down}$. The upstream electron heating is assumed to be null.

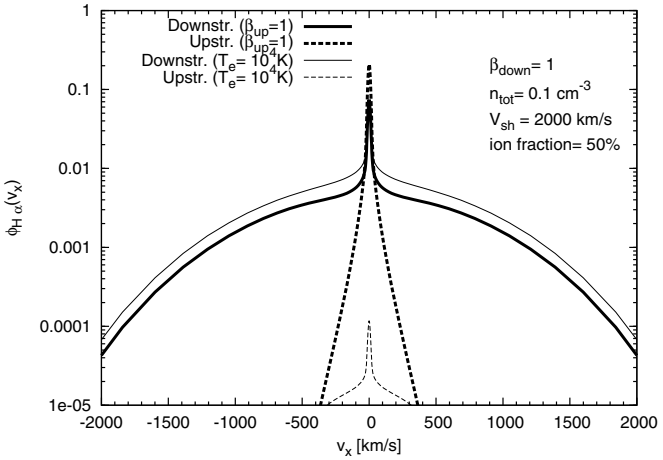

Figure 7. Volume-integrated Hα emission from downstream (solid lines) and upstream (dashed lines) for two extreme cases of upstream electron heating: thin lines refer to the case with constant upstream electron temperature, $T_e = 10^4$ K, while thick lines are computed for complete equilibration $\beta_{\rm up} = 1$. The value of downstream equilibration is fixed to $\beta_{\rm down} = 1$ for both cases.

observed: this occurs because electrons contribute to ionize hot hydrogen atoms. Also the width of the broad component decreases because a fraction of the protons' thermal energy is transferred to electrons, hence the proton temperature decreases. The narrow component, on the other hand, is only slightly affected by variations of $\beta_{\rm down}$. Its intensity increases when $\beta_{\rm down}$ goes from m_e/m_p up to $\sim$0.01, while for larger values it remains constant. In Figure 6, we only consider the effect of electron–ion equilibration downstream, while the electron temperature upstream is taken constant and equal to 10^4 K. The effect of electron heating upstream can be appreciated by looking at Figure 7, where we plot separately the volume-integrated emission from upstream and downstream assuming FE downstream, but distinguishing the NE and the FE cases upstream. The FE case shows that the total upstream emission is comparable to the downstream one, but has a very different line profile, which strongly departs from a Gaussian shape. Moreover, no broad line comes from the upstream.

In order to perform a more quantitative study of the Hα emission with the aim of extracting independent information from the three components, we decide to fit the whole line profile using three Gaussian curves. Some examples of best-fit profiles are shown in Figures 8 and 9 for the NE and the FE cases, respectively. The first point to notice is that the shape of both the broad and intermediate components slightly departs, in general, from a perfect Gaussian profile. This is especially true for the NE case and for a shock speed value below 2500 km s^{-1} (see upper panels of Figure 8). On the other hand when the shock speed and/or the electron–ion equilibration level increase, the quality of the fit improves noticeably. We note that the deviation of the broad component from a pure Gaussian profile was already pointed out by Heng & McCray (2007).

Using the three-Gaussian fit, we extract the FWHM of all three lines, which provides several pieces of information. The first remarkable result is that the width of the narrow component does not change significantly varying the shock speed and the initial ionization fraction. Its value is always $\sim$21 km s^{-1}, which corresponds to a population of atoms with a temperature of 10^4 K. This result implies that the neutral-induced precursor does not affect at all the narrow line width, which is only determined by the hydrogen temperature at upstream infinity. This is a consequence of the fact that the precursor length is smaller than the CE interaction length of cold hydrogen atoms in the upstream, irrespective of $V_{\rm sh}$ and other ambient parameters. This result is particularly important because it demonstrates that the neutral precursor cannot be responsible for the anomalous narrow-line component detected from several SNR shocks, which have an FWHM as large as $\sim$30–50 km s^{-1}.

Concerning the broad and the intermediate components, their FWHM are shown in the upper and lower panel of Figure 10, respectively. As usual we plot the results for the NE and FE cases plus some intermediate cases for the electron–ion equilibration level. Our results for the FWHM of the broad component are in good agreement with previous calculations (e.g., Smith et al. 1991). The only exception concerns the NE case, which departs from the general trend for $V_{\rm sh} < 2500$ km s^{-1}. This behavior does not have a direct physical meaning and, as already noticed, is rather due to the particularly bad quality of the fit in this region of the parameter space. We remark that the quality of the fit rapidly improves for larger value of β, and the broad line width resulting from the fit becomes very close to the actual width when $\beta_{\rm down} \gtrsim 0.01$.

As first pointed out by Chevalier et al. (1980), the FWHM of the broad line is a direct measurement of the proton temperature downstream. As a consequence it only depends on the values of $V_{\rm sh}$ and $\beta_{\rm down}$. This result can be easily understood using a plane-parallel shock model for a totally ionized plasma, which gives a proton temperature equal to $T_i = 3m_p V_{\rm sh}^2/16(1 + \beta_{\rm down})k_B$, where m_p is the proton mass and k_B the Boltzmann constant. As we showed in Paper I, this result still remains a good approximation when the plasma is only partially ionized and the neutral return flux is taken into account. On the other hand, a deviation of the proton temperature from this estimate can be induced by the presence of helium. In fact, immediately downstream of the shock, helium nuclei thermalize at a temperature $m_{\rm He}/m_p$ times larger than the protons' one. If helium and protons thermalize at the same temperature on a length scale smaller than the excitation length scale, the mean temperature of hot hydrogen produced by CE with hot protons is larger than the prediction without helium. As a consequence the FWHM is expected to be larger. Indeed, the presence of helium was taken into account by van Adelsberg et al. (2008), which found for the broad component an FWHM about 15%–18% larger than the one found in our calculations.

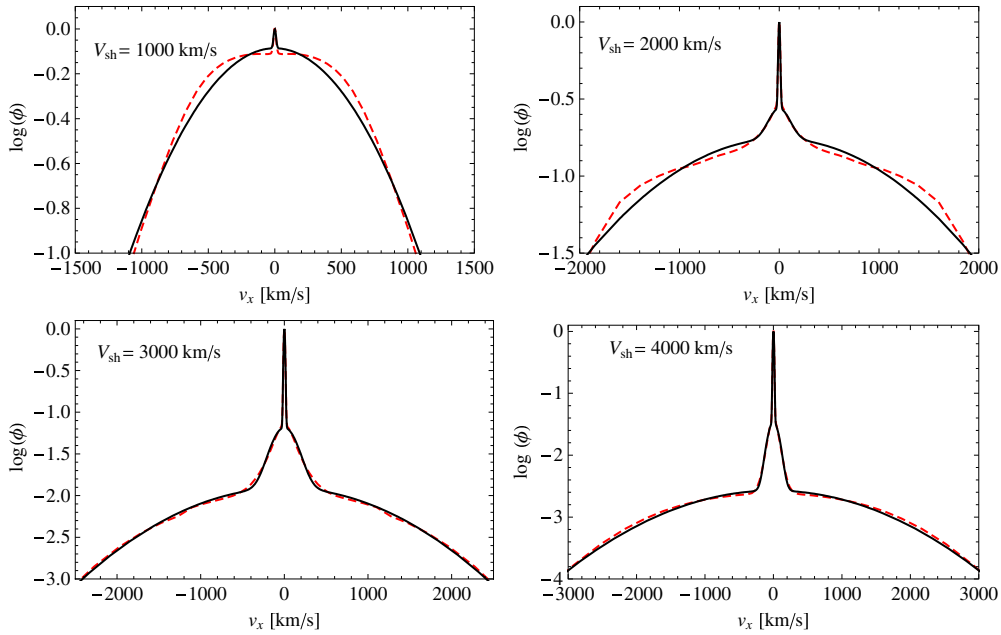

Figure 8. Examples of fits with three Gaussian curves for different values of the shock velocity, in the NE case. The dotted lines represent the emission computed with our kinetic model, while the solid line is the best fit. The quality of the fit increases for larger values of V_{sh}. Note that all profiles are normalized such that the peak value is equal to 1.

(A color version of this figure is available in the online journal.)

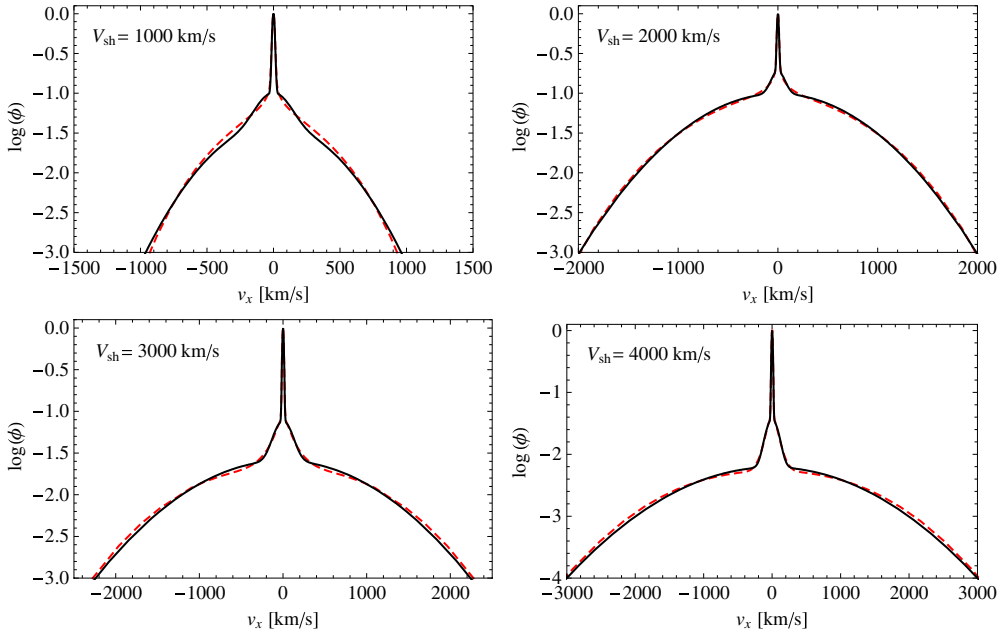

Figure 9. Same as Figure 8 but for the FE case.

(A color version of this figure is available in the online journal.)

Let us now consider the width of the intermediate component (lower panel of Figure 10). In this case, for 1000 km s^{-1} < V_{sh} < 5000 km s^{-1}, the FWHM ranges between 100 and 300 km s^{-1}. A peak is present for 2000 km s^{-1} < V_{sh} < 3500 km s^{-1}, depending on the level of electron–ion equilibration. Once again, we notice that for V_{sh} < 1500 km s^{-1} the FWHM obtained from the fit procedure is not well determined in that the intermediate component departs from a pure Gaussian shape. Moreover, the emission due to the broad component becomes much larger than the contribution of the intermediate one, which, in turn, becomes less distinguishable.

Observational evidences, compatible to what we call here *intermediate component*, have been reported in several works, even if such evidences have never been related to the neutral-induced precursor. The most interesting case is the Hα line profile detected from the "Knot g" of the Tycho's SNR by Ghavamian et al. (2000). There, an observation of Hα emission performed with high spectral resolution suggests the presence of two superimposed lines: a narrow one, with an FWHM of ∼44 km s^{-1}, plus a second, less pronounced line, whose FWHM is ∼150 km s^{-1}. Such a width is fully compatible with the FWHM of the intermediate component resulting from our

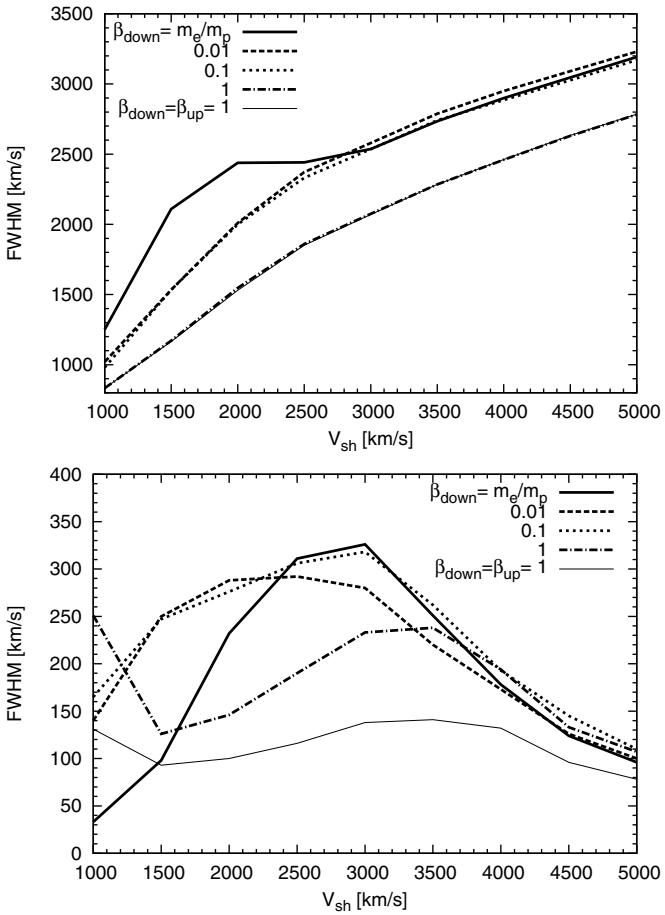

Figure 10. FWHM for broad (upper panel) and intermediate components (lower panel) resulting from the fit of total Hα emission with three-Gaussian distributions.

calculations. On the other hand, it is important to stress that the *Knot g* is a complex region where density variations of the ISM produce a non-spherical shock, hence the observed line profile could also result from projection effects. For this reason observations with better spatial and spectral resolution are required in order to disentangle geometrical effects from physical effects. The Balmer emission detected from Tycho is not an isolated case. Several spectra observed from Balmer-dominated shocks show evidence of narrow Hα lines with non-Gaussian "wings" (see, e.g., Smith et al. 1994). We suggest that such wings could be the signature of the intermediate component.

In spite of this interesting connection, in the present work we avoid performing a detailed comparison between theoretical predictions and observations. The reason is that although the calculations presented here represent a considerable step forward in the description of collisionless shocks in partially ionized media, they still remain incomplete. Aside from some minor complications that need to be taken into account (like the presence of helium or projection effects arising from deviations from plane geometry), a major role in determining the shape of the Hα line is played by the presence of CRs, which are not yet included here. In fact, it is widely accepted that efficient CR acceleration changes the global shock structure, generating an upstream precursor, that is, to some extent, similar to the neutral-induced precursor but develops on a different length scale. Effects induced by CRs could be especially relevant for the Tycho's SNR, which has been suggested to accelerate CRs efficiently (Morlino & Caprioli 2012). In passing we notice that the efficient acceleration of CRs is the most plausible explanation of the relatively wide narrow Balmer line found in Tycho (FWHM of $\sim$44 km s^{-1}).

It is worth noticing that alternative explanations for the non-Gaussian wings have also been proposed. For example, Raymond et al. (2008) suggest that deviations from the Gaussian profile could be the result of a non-Maxwellian proton distribution downstream. In fact, neutral atoms that become ionized could settle into a bi-spherical distribution (similar to that of pickup ions in the solar wind) that would then introduce a non-Gaussian contribution to the line core. We recall that in the present work, as well as in Paper I, we do not include such an effect, but we assume that, soon after being ionized, atoms thermalize with the rest of ions.

4.3. Hα Emission from the Upstream

This section is devoted to highlighting some features of the Hα emission from the upstream region. This is a crucial observable in order to understand the effects produced by CR acceleration, as we will show in a forthcoming paper. In the near future, observations could reach good enough spatial and spectral resolution so as to provide detailed spectra at different distances from the shock position, which makes the exercise of analyzing the details of the emission from the upstream especially interesting.

As we already showed in Figure 2 the upstream region could radiate up to 40% of the total Balmer emission in the case of full electron–ion temperature equilibration. On the other hand, if $\beta_{\rm up} \lesssim 0.01$ the upstream emission drops below 1% of the total. The line profile in the upstream emission is quite different from the one produced in the downstream region. In fact only the narrow and the intermediate lines are present. This is clearly shown in Figure 11 where the upstream line profile at different distances from the shock is shown for the cases of FE and partial equilibration and for $V_{\rm sh} = 2000$ and 4000 km s^{-1}. We chose the following distances: $z = 1\times, 2\times$, and $5 \times L_{\rm mfp}$, where $L_{\rm mfp} = 1/(\sigma_{\rm ce} n_{\rm tot}) \sim 10^{16}$ cm, and the CE cross section is approximated as $\sigma_{\rm ce} \sim 10^{-15}$ cm^2. As we move far away from the shock, the FWHM of the intermediate line decreases as a consequence of a reduction of the temperature in the precursor, while the narrow line has always the same FWHM. The total emission falls down at a distance of $\sim$few $L_{\rm mfp}$. This distance corresponds to the position where the electron temperature falls below the threshold of $\approx 1.5 \times 10^5$ K discussed in the second paragraph of Section 4.1. This point moves further from the shock for larger values of $\beta_{\rm up}$ as can be clearly seen in Figure 12, where we plot the integrated line emission as a function of the position only in the upstream, distinguishing the contribution of the narrow and intermediate line and for different values of the shock velocity. When we have FE the contribution of the intermediate line is always smaller than that of the narrow line, but for lower equilibration levels the ratio of intermediate over narrow emission increases and for $\beta_{\rm up} = 0.1$ the two lines contribute at roughly the same level. These findings are summarized in Figure 13.

4.4. Simulated Observations

Although the three-Gaussian fit presented in Section 4.2 catches the essence of the expected distortions in the Balmer lines, it does not reflect the whole complexity involved in fitting observed Hα line profiles. Actual data are affected by a number

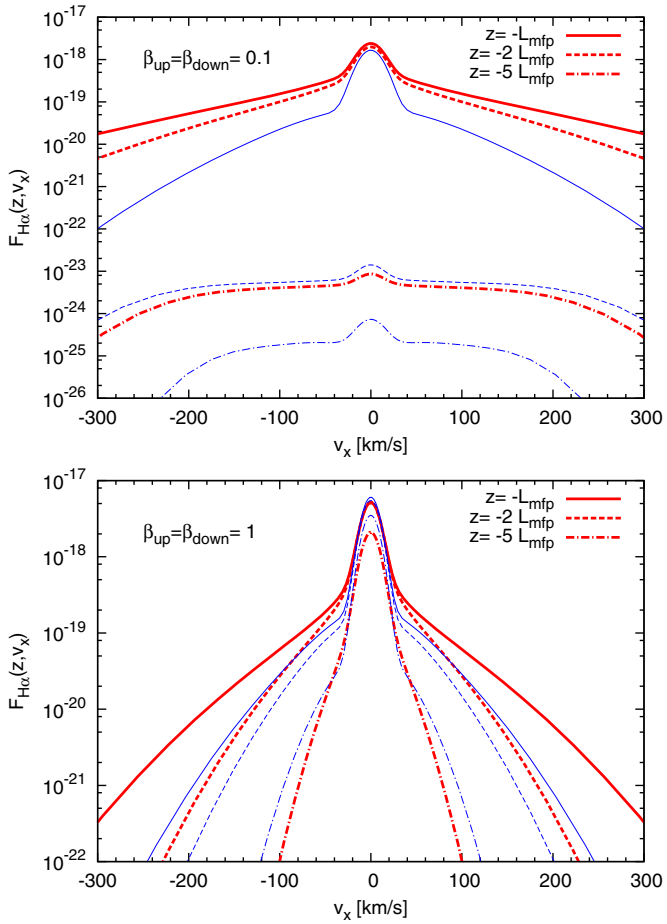

Figure 11. Emissivity profile at three different locations in the upstream for partial equilibration, $\beta_{up} = \beta_{down} = 0.1$ (upper panel), and FE, $\beta_{up} = \beta_{down} = 1$ (lower panel). Thick (red) lines show the case for $V_{sh} = 2000$ km s^{-1} while thin (blue) lines are for $V_{sh} = 4000$ km s^{-1}.

(A color version of this figure is available in the online journal.)

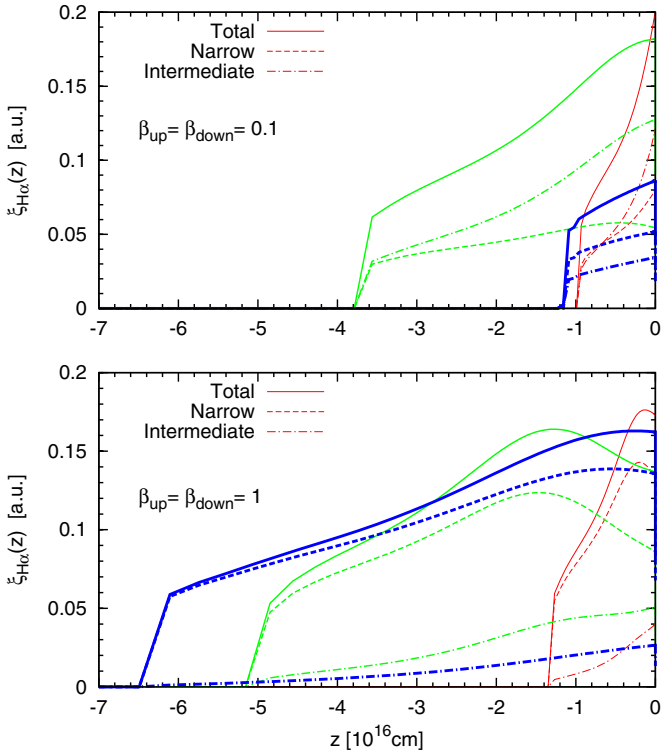

Figure 12. Spatial emissivity profile of the Hα line in the upstream. The upper panel shows the case of partial electron–ion equilibration with $\beta_{up} = \beta_{down} = 0.1$ while the lower panel shows the FE case. Dashed and dot-dashed lines show the contribution of narrow and intermediate lines, respectively, while the solid line is the total emission. The line thickness (and color) distinguishes the different shock velocities: 1000 (thin-red), 2000 (middle-green), and 4000 km s^{-1} (thick-blue).

(A color version of this figure is available in the online journal.)

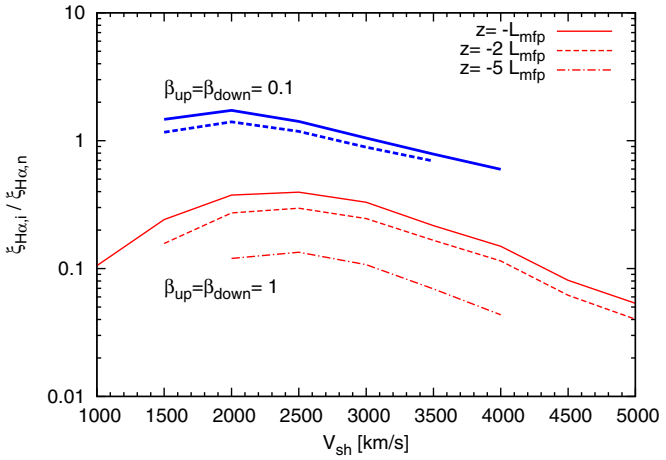

Figure 13. Ratio of the intermediate to narrow Hα emission at different locations in the upstream, as a function of the shock velocity. Different line shapes correspond to different locations, as indicated in the label. Thick (blue) lines show the partial equilibration case, while thin (red) lines show the FE case. The region of the parameter space where the Hα emission drops at a level of 10^{-4} times the peak value are not shown in the plot. For example, for the case of partial equilibration at a distance of $5L_{mfp}$ the emission is always below this threshold.

(A color version of this figure is available in the online journal.)

of instrumental and statistical issues, the most obvious of which (and the only ones that we will investigate here) are the limited spectral resolution of the instrument, the Poisson noise of the line photons themselves, and any additional photon noise, either due to the astronomical or to the instrumental background.

For the simulations presented here we have used the line profile computed for $V_{sh} = 3000$ km s^{-1} (and with an ion fraction of 50%), $\beta_{down} = m_e/m_p$, T_e(up)$= 10^4$ K. This situation is the one plotted as a dotted line in the upper panel of Figure 4.

As for the observational parameters, we will adopt a published observation of an Hα line profile in SN 1006 (Ghavamian et al. 2002) as the reference for the instrumental parameters as well as for the flux levels. In that observation, the instrumental resolution is 4.5 Å, corresponding to 205 km s^{-1}, while the dispersion per pixel is 0.27 times the resolution; the total number of photons measured in the line is about 10^9 (for a 140 minute integration time, with a 4 m class telescope), while the background noise level is about 3000 photons Å^{-1}: these photon numbers are for the whole spectrograph slit and integration time, as specified by Ghavamian et al. (2002).

Figure 14 shows the results of a two-Gaussian fit to simulated data, obtained combining the model with the instrumental parameters mentioned above. As shown by the residuals, in this case the quality of the observation is not sufficient to investigate details, beyond the mere separation of a narrow and a broad component.

We have then explored several combinations of the observational parameters, focusing on the spectral resolution (expressed

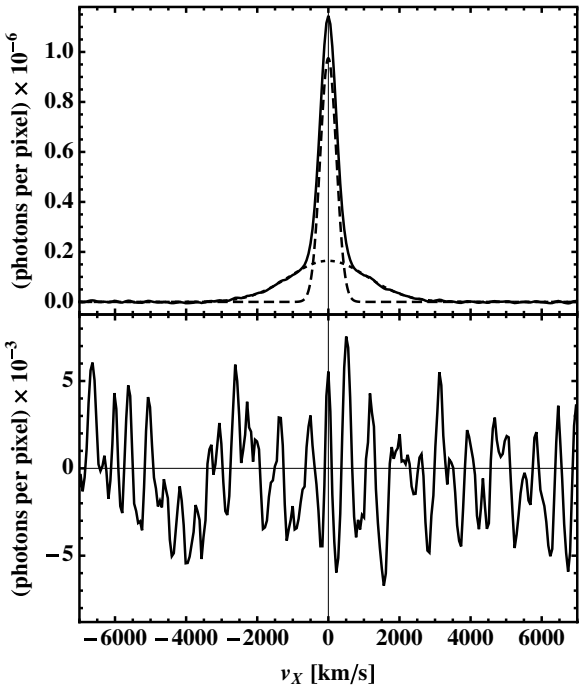

Figure 14. Results of a two-Gaussians fit to a simulated line profile, obtained by downgrading our model with a typical instrumental resolution and photon noise, and adding Poisson noise (see the text for details). The upper panel shows the simulated data (solid line), together with the best-fit narrow-line (dashed line) and broad-line (dotted line) components; while the lower panel shows the residuals after subtraction of the best-fit solution.

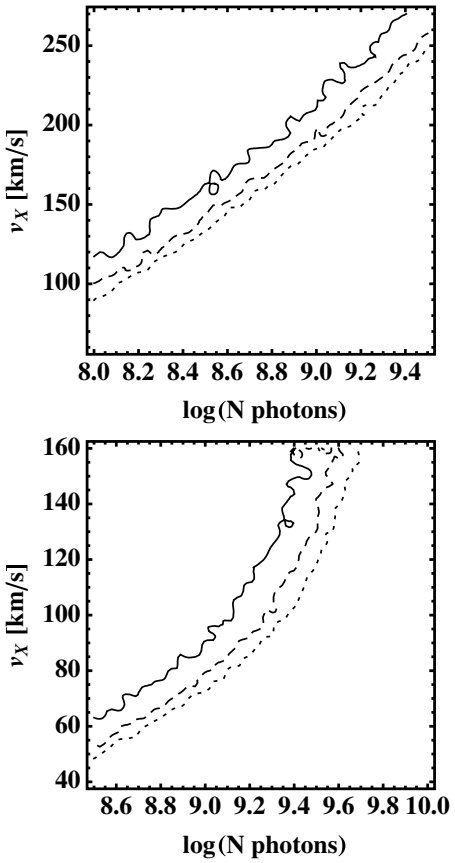

Figure 15. Behavior of the two-Gaussian (upper panel) and three-Gaussian (lower panel) fits on simulated data obtained starting from our model. We have investigated the parameter plane $\log_{10}(N_{\rm phot})$–$v_{\rm res}$. The three contours in each panel, drawn respectively as a solid, a dashed, and a dotted line, indicate the 1σ, 2σ, and 3σ confidence level. The contours are obtained by interpolating over a 40×40 data grid, each point of which is an average value of 50 independent simulations. These plots show that only on the lower right side of the panels the quality of the observations is good enough to allow outlining deviations from, respectively, a three- or two-Gaussian profile.

in terms of velocity resolution, $v_{\rm res}$) and on the photon statistics (expressed in terms of the total number of photons in the line, $N_{\rm phot}$). As for the instrumental dispersion per pixel, we have kept the ratio of 0.27 times the resolution, as in Ghavamian et al. (2002), while we have usually adopted the background noise level given above. We have also tried with a much lower background noise level, but, of course, even in this case, the noise component associated with the photons of the line itself cannot be eliminated.

We have used a grid of simulations to investigate, on the $\log(N_{\rm phot})$–$v_{\rm res}$ parameter plane, the behavior of two-Gaussian and three-Gaussian fits. In both cases we have chosen a grid of 25×25 points, suitably positioned in the parameter plane. In order to minimize the "noisy" look in the figure (a natural consequence of the fact that each simulation includes random noise), we have performed a large number (100) of simulations for each point; out of them, we have discarded the five cases with the highest χ^2 value as well as the five ones with the lowest χ^2 value, and we have then taken the average χ^2 of the remaining ones. The results are shown in Figure 15.

As a result, for our model, we may see that, for a line photon statistics of about 10^9 photons, a spectral resolution better than about 180 km s^{-1} is required to show (at a 3σ confidence level) that a two-Gaussian fit is not adequate; while a resolution better than about 70 km s^{-1} is required to challenge the three-Gaussian fit. Even if having more photons does matter, in general the photon statistics does not seem to be a parameter as crucial as the spectral resolution. Of course, in order to resolve the narrowest spectral component a considerably higher resolution is required; otherwise, it will be detected only as an "unresolved spectral component."

4.5. Line Intensity Ratios

Another observable that may be useful in order to constrain shock parameters is the ratio between the intensities of broad and narrow components, I_b/I_n. This information is usually used in combination with the FWHM of the broad component, in order to infer simultaneously both $V_{\rm sh}$ and the level of electron–ion equilibration downstream (Heng 2009). The presence of the neutral-induced precursor complicates a bit this exercise because the upstream equilibration also plays a role, as we show below.

At this point we need to comment on an observational caveat. When Balmer emission is observed with a high spectral resolution, in order to resolve the narrow component, usually the broad component is not detected due to the high spectral dispersion (see, e.g., Ghavamian et al. 2000). In order to measure the intensity of the broad component, which allows one to estimate the I_b/I_n intensity ratio, observations must be performed instead with a lower spectral resolution, typically equivalent to a velocity resolution $\Delta v \sim$ 100–300 km s^{-1}; but this does not allow resolving simultaneously all three components, because at such resolution the intermediate component cannot be distinguished from the narrow one, as they appear as a single line. As a consequence, in order to provide an estimate of I_b/I_n, we first convolve the line profile obtained by our kinetic calculation,

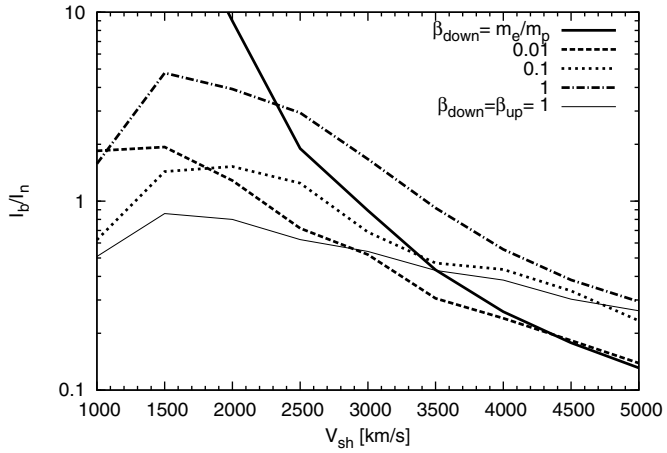

Figure 16. Ratio of the broad to narrow Hα emission vs. shock velocity after the convolution with experimental velocity resolution of $\Delta v = 150$ km s^{-1}. Different lines represent different cases of electron–ion equilibration efficiency. Thick curves all assume non-equilibrium upstream, while the thin curve shows the FE case.

with the typical instrumental resolution, Δv. Then we fit the convolved emission with a two-Gaussian profile, evaluating both I_b and I_n from the fitting curves. We choose $\Delta v = 150$ km s^{-1}, which corresponds to a wavelength resolution of $\Delta\lambda = 3.3$ Å.

The results are shown in Figure 16, where different lines represent different assumptions for the electron–ion equilibration level. The qualitative behavior is similar to that predicted by previous studies (Smith et al. 1991; Heng & McCray 2007), even if some differences can be noted. Our results are, in general, a factor 2–3 larger than predicted by Smith et al. (1991) (see their Figure 8). Their equilibrated case (which corresponds to our dot-dashed line) peaks at $V_{sh} = 2000$ km s^{-1} and is $I_b/I_n \simeq 2$ while our curve peaks at $V_{sh} \simeq 1500$ km s^{-1} with $I_b/I_n \simeq 5$. In fact, it is rather difficult to perform a close comparison between the ratios computed by different authors, because of substantial differences in the model assumptions, in the methods used, in the assumed chemical composition, and even in the cross sections adopted for the various processes; therefore, we take the above level of differences as acceptable.

From the observational point of view, in all the SNRs for which I_b/I_n has been measured, an intensity ratio above 1.2 has never been seen, while in most cases it falls below unity (see, e.g., Heng & McCray 2007). If we assume NE upstream, this result suggests an intermediate value for the electron–ion equilibration efficiency downstream. On the other hand, we also see that the FE model (both upstream and downstream) predicts an intensity ratio <1 for all shock velocities considered. Unfortunately, for given values of I_b/I_n and V_{sh} there is a degeneracy for the values of β_{up} and β_{down}.

Moreover, the trend of I_b/I_n with respect to the electron–ion equilibration is not monotonic. As first noticed by Smith et al. (1991), NE and FE cases do not represent the extreme values of the intensity ratio. We see, in fact, that for intermediate values of β_{down}, I_b/I_n drops below the equilibrated case $\beta_{down} = 1$.

5. CONCLUSIONS

In this paper we computed the Hα emission produced by a collisionless shock that propagates into a partially ionized medium. In order to do this, we first derived the evolution of the various species across the shock, by using the kinetic model developed in Paper I. This model applies to plane-parallel non-radiative shocks in the steady state where ions are treated as a fluid, while neutral particles are described using the full three-dimensional velocity distribution function. On top of this solution we then computed the Balmer emission produced by collisional excitation of hydrogen atoms with both ions and electrons, as well as by CE events leading to neutrals in excited states. Results for the spatial emission and for the line profile of Hα are presented for a shock seen edgewise, varying the shock speed, the initial ionization fraction, and the electron–ion equilibration level.

According to the traditional picture (Chevalier & Raymond 1978), the Hα profile detected from Balmer-dominated shocks usually consists of two components: a narrow one, whose width reflects the temperature of the upstream medium, and a broad one, due to neutrals that have undergone CE with hot protons in the downstream region.

This picture is however an oversimplification of what happens in reality, mainly for two reasons: (1) it assumes that neutrals can be described as a fluid, namely, with Maxwellian velocity distributions; (2) it does not take into account the effect induced by the neutral precursor. In fact, the latter point is a natural consequence of the former one: already in Paper I we showed that, for a wide range of shock velocities, a fraction of the hot neutrals produced downstream can recross the shock toward upstream, giving rise to a neutral return flux, and that the interaction of these neutrals with the upstream ions produces a precursor region where the incoming plasma is heated and slowed down. In this paper, we have shown that the neutral-induced precursor is responsible for the production of a new Hα line component, whose width is intermediate between the narrow and the broad lines, being around a few hundreds of km s^{-1} for a shock speed of a few thousands of km s^{-1}. This intermediate line is due to cold hydrogen atoms that have undergone CE with warm protons in the neutral-induced precursor, hence its width reflects the mean temperature of the precursor. In addition, we found that the profiles of the intermediate and broad-line components may deviate from pure Gaussians, and that these deviations could be detected by carrying out observations of suitably high quality.

A natural question to ask is whether the heating produced in the neutral precursor could explain the anomalous width of narrow lines, which has already been observed in some Balmer filaments associated with several SNR shocks (Smith et al. 1994; Hester et al. 1994). Our results show that this is not the case: the bulk of incoming neutrals does not interact with ions in the neutral precursor because its extent, which corresponds to the interaction length of the returning neutrals, is much smaller than the CE length of the incoming neutrals. Instead, as we already discussed, the fraction of incoming neutrals interacting with ions in the precursor will give rise to the intermediate Hα line. Therefore, we conclude that other mechanisms, such as for instance a CR-induced precursor, should be invoked to explain an anomalous width of the narrow-line component.

Remarkably, some observations point toward the existence of intermediate lines compatible with our predictions: narrow lines detected from Tycho and from other SNRs show non-Gaussian wings which could be explained with the existence of a third line component. At the moment this result must be taken with care because projection effects could also be responsible for the observed line profiles. Better spatial and spectral resolution are needed to disentangle these effects. Unfortunately, the majority of these observations do not have the spectral resolution required to carry out a satisfactory three-component fit. In

order to estimate the experimental requirements necessary to identify the intermediate line, we compared our theoretical Hα profile with simulated observations, which take into account both instrumental resolution and Poisson noise of the line photons. As a result, for a typical line photon statistics of about 10^9 photons, a spectral resolution better than $\sim$70 km s^{-1} is required to separately identify all three components.

The presence of the intermediate line component may also affect the evaluation of the broad to narrow line intensity ratio, I_b/I_n. This quantity is usually used together with the broad line width, in order to estimate the level of electron–ion temperature equilibration in the post-shock region. Evaluation of I_b/I_n is usually done from observations with resolution $>$100 km s^{-1}, necessary to detect both the narrow and the broad lines.

This implies that the intermediate line is not resolved and that its emission contributes to the observed narrow line intensity. We have included this effect in the evaluation of I_b/I_n, and have shown how this ratio changes varying the electron–ion equilibration downstream. As already pointed out by several authors, if efficient electron–ion equilibration occurs downstream, the width of the broad line is reduced because a fraction of the kinetic energy of incoming protons is transferred to electrons.

In addition to the effects produced by electron–ion equilibration downstream, we investigated what happens if equilibration also occurs in the precursor region. Interestingly, we showed that, increasing the efficiency of equilibration beyond a few percent, electrons can collisionally excite hydrogen atoms, giving rise to Balmer emission also from the precursor region. For $V_{\rm sh} \approx 2500$ km s^{-1}, if equilibration is complete ($T_e = T_p$), the emission from the precursor can contribute up to $\sim$40% of the total Hα emission. This result can be instrumental to explain the results recently published by Lee et al. (2010). They observe the Eastern limb of Tycho's SNR, finding a gradual increase of Hα intensity just ahead of the shock front, which they interpret as emission from a thin shock precursor. They estimate that the precursor emission may contribute up to 30%–40% of the total narrow component emission and suggest that the precursor is likely due to CRs. In light of our results, it is clear that a correct interpretation of the pre-shock Hα emission requires also the evaluation of the emission produced by the neutral-induced precursor.

In a forthcoming paper, currently in preparation, we will describe the theory of collisionless shocks in partially ionized media in the presence of accelerated particles that exert a pressure on the incoming ions. In other words, we will generalize the nonlinear theory of particle acceleration in collisionless shocks to include the neutral return flux discussed in Paper I. In the same paper, we will calculate the shape of the Balmer lines as they are affected by accelerated particles, and show how to use the widths of the narrow, intermediate, and broad components of the Balmer line as tools to measure the CR acceleration efficiency in SNRs.

We thank an anonymous referee for his/her valuable suggestions which allowed us to improve the quality of the present work. We are very grateful to Kevin Heng for providing some of the cross sections used in this work. Our work is partially funded through grants PRIN-INAF 2010 and ASTRI.

REFERENCES

Balança, C., Lin, C. D., & Feautier, N. 1998, J. Phys. B, 31, 2321
Barnett, C. F., Hunter, H. T., Fitzpatrick, M. I., et al. 1990, Collisions of H, H2, He and Li Atoms and Ions with Atoms and Molecules (Rep. ORNL-6086/V1; Oak Ridge, TN: Oak Ridge National Laboratory)
Belkić, D., Gayet, R., & Salin, A. 1992, At. Data Nucl. Data Tables, 51, 59
Blasi, P., Morlino, G., Bandiera, R., Amato, E., & Caprioli, D. 2012, ApJ, 755, 121
Bray, I., & Stelbovics, A. T. 1995, Advances in Atomic, Molecular, and Optical Physics, Vol. 35 (New York: Elsevier), pp 209–54
Chevalier, R. A., Kirshner, R. P., & Raymond, J. C. 1980, ApJ, 235, 186
Chevalier, R. A., & Raymond, J. C. 1978, ApJ, 225, L27
Ghavamian, P., Laming, J. M., & Rakowski, C. E. 2007, ApJ, 654, L69
Ghavamian, P., Raymond, J., Hartigan, P., & Blair, W. B. 2000, ApJ, 535, 266
Ghavamian, P., Raymond, J. C., Smith, R. C., & Hartigan, P. 2001, ApJ, 547, 2005
Ghavamian, P., Winkler, P. F., Raymond, J. C., & Long, K. S. 2002, ApJ, 572, 888
Harel, C., Jouin, H., & Pons, B. 1998, At. Data Nucl. Data Tables, 68, 279
Helder, E., Vink, J., Bassa, C. G., et al. 2009, Science, 325, 719
Heng, K. 2009, PASA, 27, 23
Heng, K., & McCray, R. 2007, MNRAS, 654, 923
Heng, K., & Sunyaev, R. A. 2008, A&A, 481, 117
Hester, J. J., Raymond, J. C., & Blair, W. P. 1994, ApJ, 420, 721
Janev, R. K., & Smith, J. J. 1993, Cross Sections for Collision Processes of Hydrogen Atoms with Electrons, Protons and Multiply Charged Ions (Vienna: International Atomic Energy Agency)
Lee, J. J., Raymond, J. C., Park, S., et al. 2010, ApJ, 715, L146
Lim, A. J., & Raga, A. C. 1996, MNRAS, 280, 103
Morlino, G., & Caprioli, D. 2012, A&A, 538, 81
Rakowsky, C. E. 2005, Adv. Space Res., 35, 1017
Raymond, J. C., Isenberg, P. A., & Laming, J. M. 2008, ApJ, 682, 408
Smith, R. C., Kirshner, R. P., Blair, W. P., & Winkler, P. F. 1991, ApJ, 375, 652
Smith, R. C., Raymond, J. C., & Laming, J. M. 1994, ApJ, 420, 286
Sollerman, J., Ghavamian, P., Lundqvist, P., & Smith, R. C. 2003, A&A, 407, 249
Tseliakhovich, D., Hirata, C. M., & Heng, K. 2012, MNRAS, 422, 2357
van Adelsberg, M., Heng, K., McCray, R., & Raymond, J. C. 2008, ApJ, 689, 1089